A 38 dB Gain, Low-Loss, Flat Array Antenna for 320–400 GHz Enabled by Silicon-on-Insulator Micromachining

Adrian Gomez-Torrent, *Graduate Student Member, IEEE*, Takashi Tomura, *Member, IEEE*, Wataru Kuramoto,
Jiro Hirokawa, *Fellow, IEEE*, Issei Watanabe, Akifumi Kasamatsu,
and Joachim Oberhammer, *Senior Member, IEEE*

Abstract—Two high-gain flat array antenna designs operating in the 320–400 GHz frequency range are reported in this article. The two antennas show the measured gains of 32.8 and 38 dBi and consist of a 16 × 16 (256) element array and a 32 × 32 (1024) element array, respectively, which are fed by a corporate H-tree beamforming network. The measured operation bandwidth for both antennas is 80 GHz [22% fractional bandwidth (FBW)], and the total measured efficiency is above −2.5 dB and above −3.5 dB for the two designs in the whole bandwidth. The low measured loss and large bandwidth are enabled by optimizing the designs to the process requirements of the silicon on insulator (SOI) micromachining technology used in this article. The total height of the antennas is 1.1 mm (1.2 λ at the center frequency), with sizes of 15 mm × 18 mm and 27 mm × 30 mm for both arrays. The antennas are designed to be directly mounted onto a standard WM-570 waveguide flange. The design, fabrication, and measurements of eight prototypes are discussed in this article and the performance of the antennas compared to the simulated data, as well as manufacturability and fabrication repeatability are reported in detail.

Index Terms—Array antennas, corporate beamforming network (BFN), silicon micromachining, silicon on insulator (SOI), submillimeter-wave (sub-mmW) antennas, terahertz (THz) radiation, waveguide arrays.

I. INTRODUCTION

WIRELESS mobile traffic keeps growing, and it is expected to reach 131 EB/month by 2024 [1]. The current trend to meet this traffic demand is to make use of the available terahertz (THz) region of the electromagnetic spectrum that will enable multi-Gbps wireless data links [2]. One of the main problems with THz links is the high atmospheric attenuation, which degrades the signal-to-noise ratio and, thus, the maximum capacity of the channel.

The gain and bandwidth of the antennas used for data links are critical parameters in order to increase the channel capacity [2], [3], which is particularly relevant in the THz range due to the higher atmospheric attenuation mentioned above. For this reason, the interest in developing high-gain and broadband antennas at frequencies above 300 GHz has increased in the last years [4]–[10].

One of the main difficulties when implementing antenna frontends in the submillimeter wave (sub-mmW) range and above is the reduced size of the wavelength that scales all components down in size. Optical systems such as reflectors or lenses, which are several wavelengths in size and do not usually require micrometer size features, are relatively easy to manufacture up to the THz range [4], [5]. Reflectarrays can be a good alternative to reflectors and can be manufactured by a lithography process at a low cost [10]; however, they have a narrow operation bandwidth and usually have low radiation efficiency.

These optical systems can achieve high-gain values and wideband operation, but they tend to be heavy, bulky, and involve careful alignment of the feed antenna. *Quasi*-optical systems have been developed as an alternative solution to optical systems [6], [7], [11]. They can integrate 1-D reflectors or lenses in parallel plate waveguide (PPW) technology, thus reducing the total volume and mass of the system but limiting the beamforming to one plane. Therefore, *quasi*-optical systems need an additional beamforming network (BFN) in PPW technology to generate a pencil-shaped beam [11], making their fabrication still challenging in the THz range.

Corporate-feed array antennas can provide high gain and broadband operation, but they require waveguide BFNs with increasing complexity as the number of elements of the array increases. The geometrical complexity of the BFNs makes their fabrication extremely challenging at THz frequencies by classic computer numerical control (CNC)-milling techniques, due to the small features and high uniformity required to achieve a good performance. Tekkouk *et al.* [8] reported on
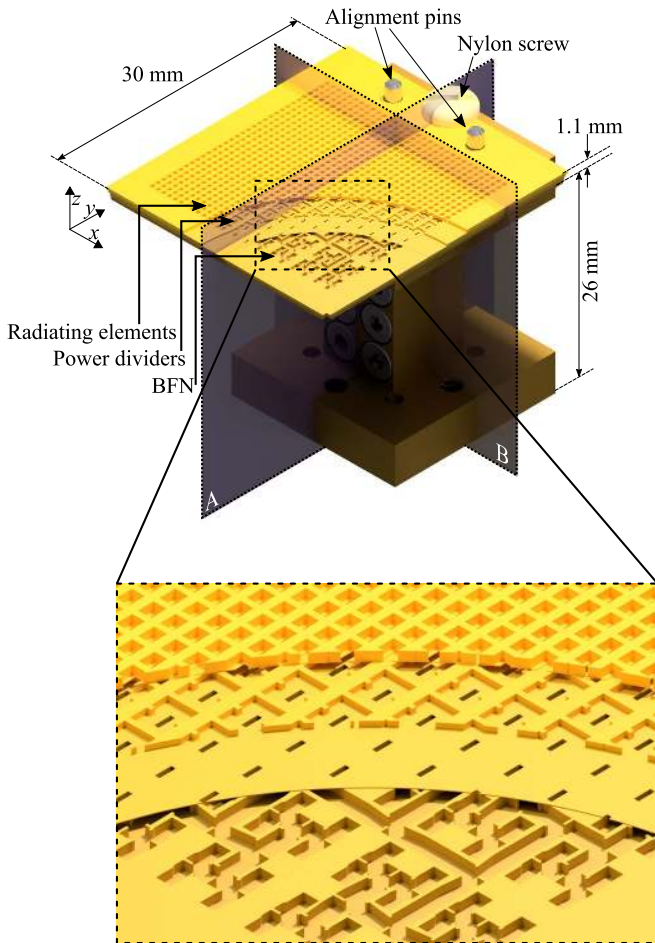
Fig. 1. Computer aided design (CAD) model of the 32×32 element array mounted on a standard WM-570 waveguide piece.
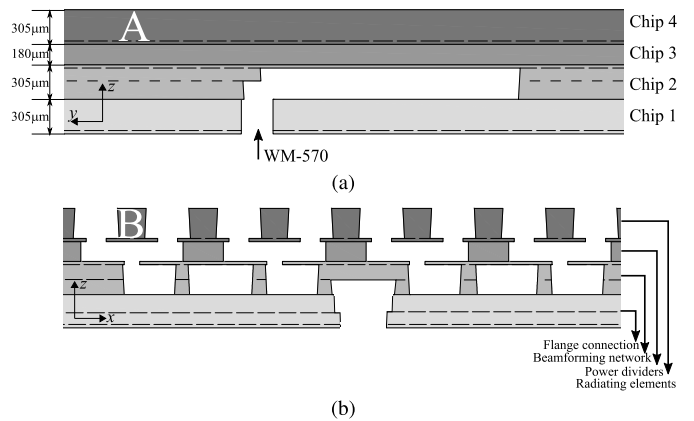

Fig. 2. Cross sections of the antenna model in Fig. 1 shows (a) input waveguide and stepped E-plane bend and (b) BFN, power dividers, and radiating elements. Dashed lines represent the different layers etched in an SOI wafer. The under etch produced by the silicon micromachining process is also represented and was considered during the design. Not to scale.

the first corporate feed array antenna above 300 GHz using silicon micromachining of standard silicon wafers. Although this approach allowed the first implementation of such an antenna, the design failed to take full advantage of the silicon micromachining technology, which resulted in increased loss and narrow bandwidth. The results not only served as a proof of concept for the use of silicon micromachining for sub-mmW array antennas but also brought out the importance of a fabrication-oriented design for waveguide components when approaching the THz range.

Silicon micromachining is a promising alternative to classical machining techniques for the implementation of waveguide components in the sub-THz frequency range. Silicon micromachining can be used to fabricate low-loss waveguides [12], high quality factor filters [13], and complex waveguide 3-D geometries such as turnstile orthomode transducers [14], switches and phase shifters [15]–[17], or antennas [5], [11], [18]. Campion *et al.* [19] have also recently demonstrated the integration of monolithic microwave integrated circuits (MMICs) in a silicon micromachined platform where the RF, IF, and dc networks are homogeneously integrated.

This article presents two high-gain array antennas in the 320–400 GHz frequency range in silicon on insulator (SOI) micromachining technology. The SOI technology allows for

multistep complex waveguide geometries [14], enabling a new design of the input transition, BFN, and radiation cell in [8] to improve the bandwidth and drastically increase the radiation efficiency. As a result, the 16×16 element array antenna presented here has double the bandwidth and a 5 dB loss reduction as compared to previous work. These significant improvements also enabled the development of a 32×32 element array, which represents the highest gain antenna in the sub-THz frequency range not based on optical systems, to the authors' knowledge. The antennas in this article can be directly mounted on a waveguide flange, avoiding the use of additional CNC-milled test fixtures or custom-made flanges that would increase the complexity, cost, and power loss of the frontend.

II. ANTENNA STRUCTURE AND DESIGN

The antenna structure, mounted on a standard test port, is shown in Fig. 1, and the cross sections of the cutting planes A and B are shown in Fig. 2. The antenna design consists of 1) a $2^n \times 2^n$ element array; 2) a corporate BFN; and 3) a standard waveguide flange interface, which are implemented in a four micromachined chip stack. All the electromagnetic simulations for the design of the antenna were carried out using the commercial software CST Studio Suite, and the radiation cell was designed by a combination of the Method of Moments and a numerical optimization genetic algorithm [20], [21].

The interface in chip 1 allows for a direct connection to a standard UG-387 flange that is aligned by using a tightly fit circular hole and an elliptical hole in order to achieve a repeatable flange-to-chip connection [22]. The stepped E-plane bend [see Fig. 3(a)] matches the standard WM-570 waveguide (570 µm × 285 µm) to the waveguide dimensions in the BFN (600 µm × 275 µm). The SOI wafer defines the height of the waveguide and it is chosen to be as close as possible to the standard waveguide height; the width of the waveguide is narrow enough to avoid the excitation of higher-order TE_{n0} modes, but it is made as wide as possible to reduce the insertion loss of the BFN. The height and length of the step are optimized to minimize the input reflections using the Trust
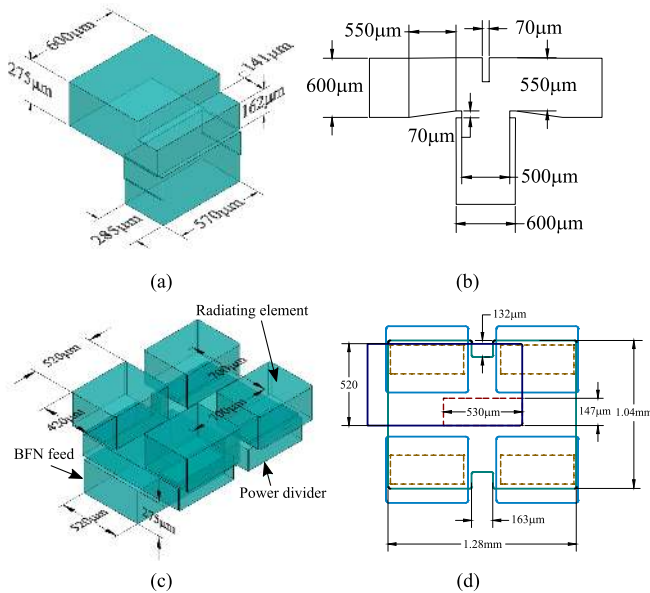
Fig. 3. Detailed geometry of the different subcomponents in the antenna frontend. (a) Input E-plane bend. (b) Power divider. (c) Perspective view of the radiation cell. (d) Top view of the radiation cell with different cavities in solid lines and coupling slots in dashed lines.
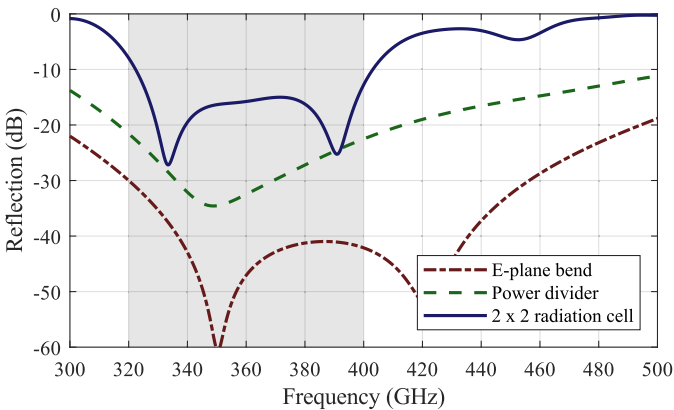

Fig. 4. Simulated input reflections for the different subcomponents in the antenna frontend. E-plane bend, power divider, and 2×2 radiation cell. The shaded gray area marks the design bandwidth.

Region Framework algorithm implemented in CST [23], which converges after seven iterations to a reflection level better than -30 dB (see Fig. 4) by setting the initial parameters to half the total height of the waveguide.

The BFN consists of an in-plane H-tree network that feeds 2^{n-2} radiation cells. The H-plane power divider was first designed to have reflections better than -20 dB in the operation bandwidth, as shown in Fig. 4. The final dimensions of the power divider are summarized in Fig. 3(b). The complete power distribution network, shown in Fig. 5, was initially simulated and finely tuned in CST Schematic. For this simulation, each of the 2^{n-2} outputs of the BFN was loaded with the simulated S_{11} of the 2×2 element radiation cell, also plotted in Fig. 4. The S-parameters of the complete antenna were then confirmed with a full-wave simulation of the whole structure.
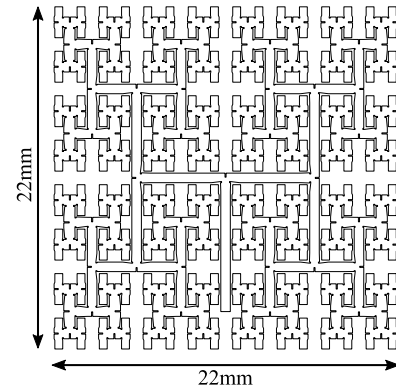

Fig. 5. Design layout of the H-tree BFN for the 32×32 ($n = 5$) antenna.

The radiation cell [Figs. 2(b) and 3(c) and (d)] is fed through a coupling slot from the power distribution network. The coupling slot in chip 2 feeds a cavity in chip 3 that acts as a power divider by uniformly exciting a set of four slots in chip 4. These slots in chip 4 couple the energy to the open ended waveguides, i.e., the radiating elements. This radiation cell, which is implemented by using only three chips, has a total number of five layers of different thicknesses doubling the operation bandwidth as compared to [8].

The coupling slots in the radiation cell have a thickness of 30 µm ($\lambda/25$ at the center frequency, 360 GHz), the layers containing waveguides have a thickness of 275 µm, and the power divider layer in chip 3 has a thickness of 180 µm. The steps for impedance matching in chips 1 and 2 have thicknesses of 144 and 162 µm, respectively. These multiple layer thicknesses were chosen to provide the best RF performance and are enabled by the SOI micromachining technology, at a low fabrication complexity. A $3°$ sidewall angle was included in all the simulations in order to consider the effects of the etching process. This value is a good initial approximation, but the actual under etch strongly depends on the mask design, and small deviations can have some influence in the input reflections of the antenna.

Finally, the complete antenna structure, including the flange, the alignment pins, and the nylon screw, was simulated using the Transient solver in CST to verify the overall performance.

III. FABRICATION

Prototypes of two antenna designs were fabricated simultaneously: a 16×16 ($n = 4$) element array antenna and a 32×32 ($n = 5$) element array antenna with expected directivity values in the central frequency ($f = 360$ GHz) from full-wave simulations of 33.5 and 39.5 dBi, respectively. Two fabrication runs were carried out, producing a total number of six 16×16 element antenna prototypes and two 32×32 element antenna prototypes.

The antennas are fabricated by deep reactive ion etching (DRIE) of SOI wafers at KTH Electrumlab, Stockholm, Sweden. DRIE is based on the Bosch process, which alternates silicon etching and passivation cycles in order to achieve large aspect ratio trenches on the wafer. The etching is performed in an STS plasma etching tool with an etch rate of 2.5 µm/min

TABLE I
SOI WAFER SPECIFICATIONS

	Handle layer thickness	Device layer thickness	Buried oxide layer thickness (BOX)
W1	$275 \pm 10\,\mu m$	$30 \pm 0.5\,\mu m$	$3\,\mu m \pm 5\,\%$
W2	$320 \pm 15\,\mu m$	$180 \pm 2\,\mu m$	$1\,\mu m \pm 5\,\%$

* Tolerances provided by the manufacturer, Utrasil LLC

and a selectivity over silicon oxide of 450:1. An endpoint detection system, based on optical emission spectroscopy, is used in the plasma chamber to detect when the buried oxide (BOX) layer of the SOI wafer is exposed to the plasma. The biasing RF power to the substrate is then switched to a pulsed mode, thus avoiding any notching effects on the bottom of the trenches. Two wafers (W1 and W2) are processed with a total number of four photolithography masks. The specifications of both SOI wafers are shown in Table I.

The multistep SOI etching process described in [14] is used to process W1. A scanning electron microscope (SEM) cross section image of the silicon oxide hard mask stack is shown in Fig. 6(a). This stack of hard masks is later used for the multistep etching of the handle layer in W1 that forms the impedance matching steps. The manufactured stepped impedance transformer in chip 1, the H-tree BFN in chip 2, and the radiating elements in chip 4 are shown in Fig. 6.

To form chip 3, see Fig. 2(a), the device layer of W2 is etched by using an oxide hard mask. The use of the device layer of an SOI wafer is preferred over a standard silicon wafer due to their better thickness tolerances and due to the difficulty to produce and handle silicon wafers with thicknesses below 200 μm. The handle layer of the SOI wafer has to be removed to release the etched structures, which is done by bulk dry etching in a fluorine plasma (SF_6). The BOX layer and oxide mask in the device layer are finally removed by wet etching in a 50% hydrofluoric acid (HF) aqueous solution.

After dry etching, the chips are cleaned in oxygen plasma and metalized with an adhesion layer of titanium/tungsten followed by 2 μm of gold in a dc magnetron sputtering tool. Each antenna is then assembled by aligning the four-chip stack under the microscope, with the aid of integrated Vernier scales, and thermal compression bonded at 200 °C for 1 h. The authors described the bonding alignment method used in this article in recent publications [11], [14], where better than 5 μm alignment accuracy is shown in the microscope images of the Vernier scales. Fig. 7 shows the manufactured antennas mounted in a standard waveguide flange.
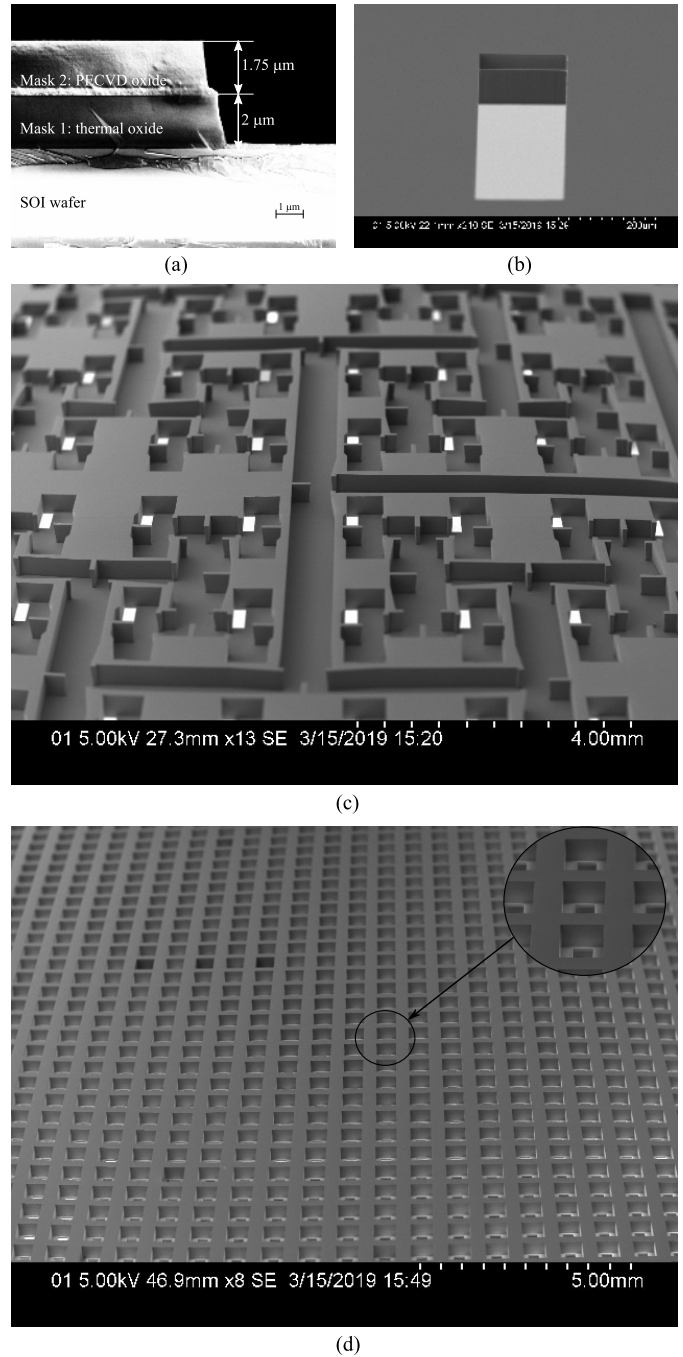
Fig. 6. SEM images of the manufactured devices. (a) Hard mask stack before DRIE process. (b) Input waveguide section with stepped impedance transformer in chip 1. (c) H-tree BFN in chip 2 showing waveguide structure and coupling slots. (d) Radiating elements with a zoomed-in view showing the coupling slots.

IV. MEASUREMENT RESULTS

The gain, half power beamwidth (HPBW), input reflections, and cardinal plane cuts of the radiation diagram were measured for all the fabricated antennas. The data obtained from the six 16 × 16 element antennas are used to evaluate the new design and fabrication technique by comparing it to the results in [8]. At the same time, the variability between different antennas is investigated to evaluate the repeatability and uniformity of the SOI micromachining process. Finally,

the measurement data of the two 32 × 32 element antennas is shown and compared to the simulation results demonstrating the feasibility of low-profile and high-gain antennas operating in the sub-THz frequency range.

The input reflections are first measured using a Rohde and Schwarz ZVA-24 VNA and a Virginia Diodes Inc. (VDI) frequency extender with WM-570 waveguide flange interface. The measured *RL* of the 16 × 16 element antennas is in good
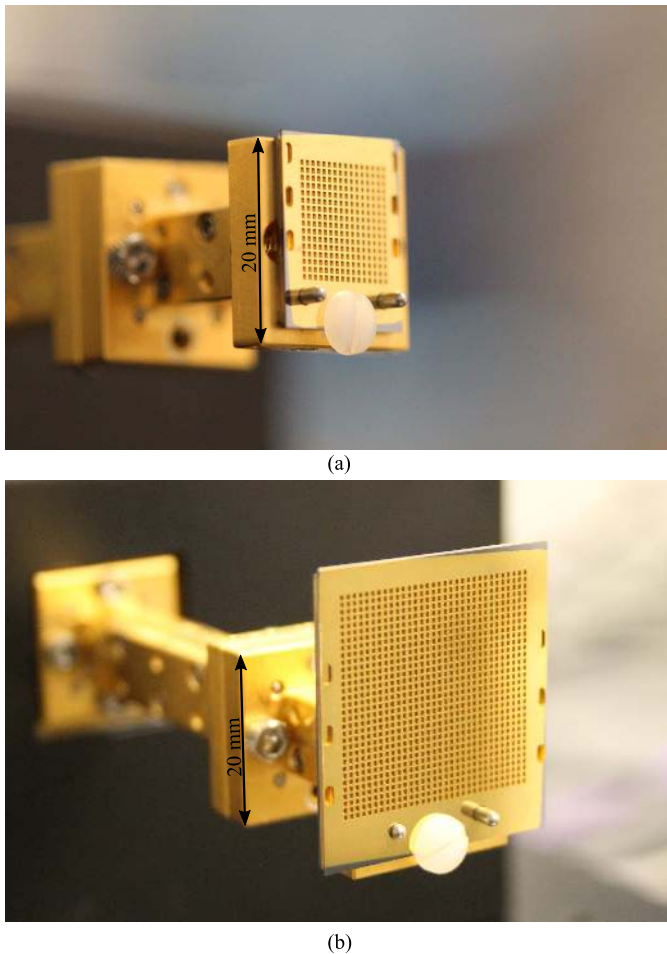
(a)

(b)

Fig. 7.   Photographs of the manufactured antennas mounted on a standard WM-570 waveguide flange. The antennas are aligned using two standard alignment pins and fixated with a nylon screw. The antenna in (a) is the 16×16 element array and the antenna in (b) is the 32×32 element array. The standard flange size is 20 mm $\times$ 20 mm.

Fig. 8.   Measured and simulated reflections for the 16×16 element array. The dashed black line shows the simulated data, and the blue solid line and shaded blue area show the mean value and the standard deviation ($\pm\sigma$) of the measured reflections for the six antenna prototypes.

Fig. 9.   Measured and simulated reflections for the two prototypes of the 32×32 element array.

agreement with the simulated data. Although the reflections go above 10 dB around 340 GHz, the average value remains below 16 dB in the design bandwidth. The RL is repeatable for all six antennas, as shown in Fig. 8, where the simulated value is plotted in dashed black lines, the mean value of the measured data for all antennas in solid blue lines, and the shaded area represents the standard deviation ($\pm\sigma$).

The input reflections of the two 32×32 element antennas are plotted in solid blue and red lines in Fig. 9. The measured data are also in good agreement with the simulations, and it is possible to observe the higher reflections around 340 GHz for this antenna design as well. This repeatable deviation from the expected results indicates that a fabrication error affects all antennas equally, hence, ruling out misalignment errors between the different chips, deviations in the height of the impedance matching steps, or chip-to-flange alignment accuracy, since these would be random errors that cannot systematically affect all the devices in the same way. One of the possible reasons is a deviation in the sidewall profile from the 3° angle considered during the design. The actual sidewall angle in the antennas was found to be 3.7°, measured
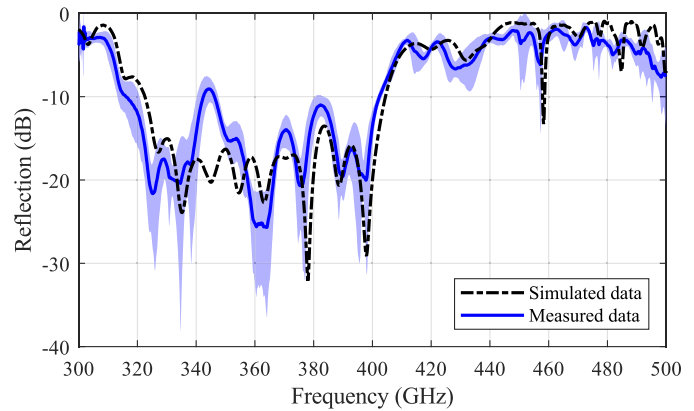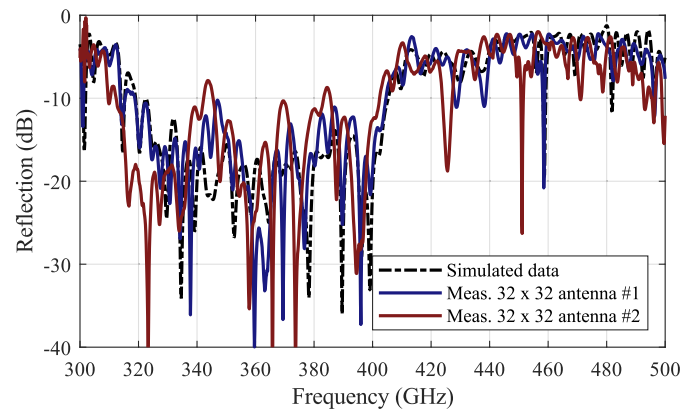
by a destructive test of one of the chips in an SEM, as shown in Fig. 10. This value can now be used for a fine optimization of the structure in a following fabrication iteration.

The gain, HPBW, and radiation patterns of the antennas were measured in the millimeter-wave anechoic chamber at National Institute of Information and Communications Technology (NICT), Tokyo. The setup consists of a 2-axis azimuth/elevation stage with the antenna under test (AUT) in the origin of rotation. A diagonal horn from VDI is used as the transmitting antenna, and it is placed at a distance of 1.2 m from the AUT in a direct illumination configuration. Two VDI frequency extenders driven by a Keysight PNA are used to measured the received power while scanning the AUT. A picture of the setup is shown in Fig. 11.

The E-plane and H-plane cuts of the radiation diagram were measured at three frequency points (325, 360, and 400 GHz). The radiation patterns of the six 16×16 element antennas in Fig. 12 show the excellent agreement of all the measurements with the simulated results. Black dashed lines show the simulated data, while the measurement data are represented as solid gray lines. The measurement data of the six prototypes has been condensed to one plot for space reasons, showing
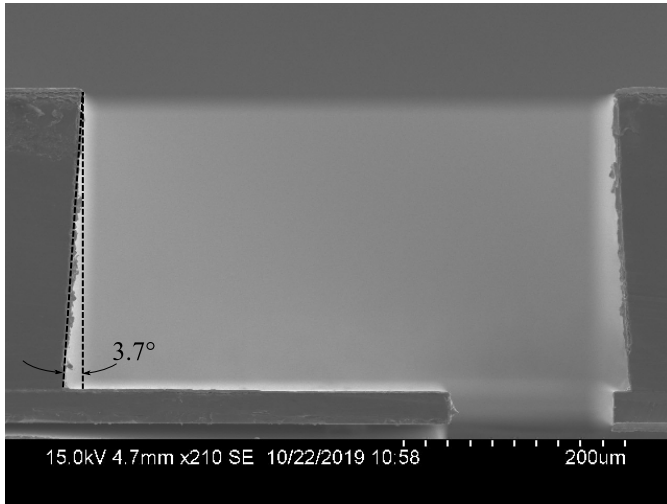
Fig. 10.   SEM image of the cross section of a waveguide showing the sidewall profile angle.
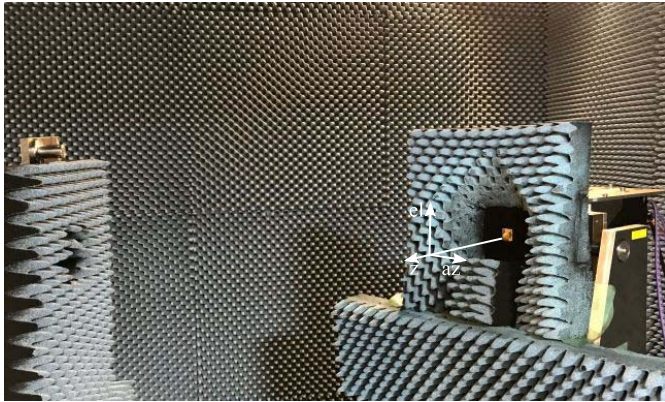

Fig. 11.   Radiation pattern measurement setup at NICT with 2-axis azimuth/elevation rotation stage.

Fig. 12.   Measured and simulated radiation patterns for the 16×16 element array. Dashed lines show the simulated data, and the solid overlaid lines show the measured data of the six manufactured prototypes.

Fig. 13.   Measured and simulated radiation patterns for the 32×32 element array. Dashed lines show the simulated data and the solid overlaid lines show the measured data of the two manufactured prototypes.

the low variability in the measured results for the different devices.

The radiation pattern cuts of the two 32×32 element antennas are shown in Fig. 13. The two solid overlaid curves show the measured data for both prototypes, in excellent agreement with the simulated data and showing the good repeatability of the fabrication process again.

The 16×16 element antennas have a measured HPBW of 4.1°–3.3° and the 32×32 element antennas of 2.1°–1.7°. The simulated and measured data are shown in Fig. 14, where the worst case deviation from the simulated data is 0.15° for the 16×16 element prototypes and 0.12° for the 32×32 element prototypes. These deviations lie below the measurement accuracy of the setup.

A 3-D pattern measurement was also performed for one of the 32×32 element antennas in order to verify the results and investigate the radiation characteristics outside the two cardinal planes. The results plotted in Fig. 15 show a very symmetric radiation pattern with sidelobe levels as expected from a uniformly excited square aperture.
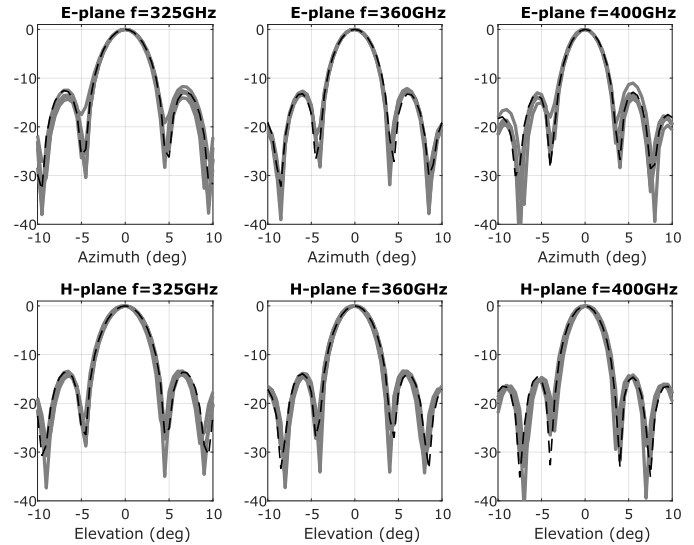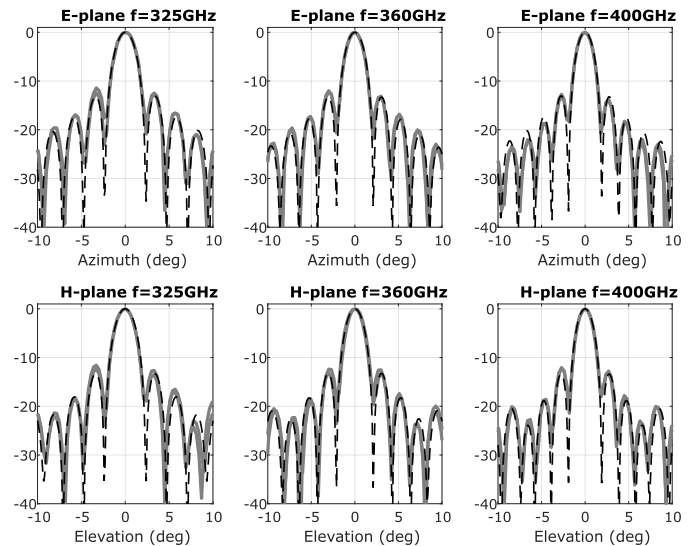
The gain of the antennas was measured using a calibrated antenna standard. Three identical CNC-milled diagonal horns, manufactured by VDI, were used to perform the three unknown antenna calibration method [24]. For the gain characterization of the micromachined antennas, two of the three horns were used as transmitting antenna and standard. Then the antenna standard was replaced with each AUT in order to characterize the gain. The measured and simulated realized gains and total antenna efficiency for the 16×16 element antennas are plotted in Fig. 16. Blue solid lines show the average measured gain and efficiency, and the shaded area represents the standard deviation ($\pm\sigma$) for each case. The measured realized gain ranges from 30 to 32.8 dBi, having
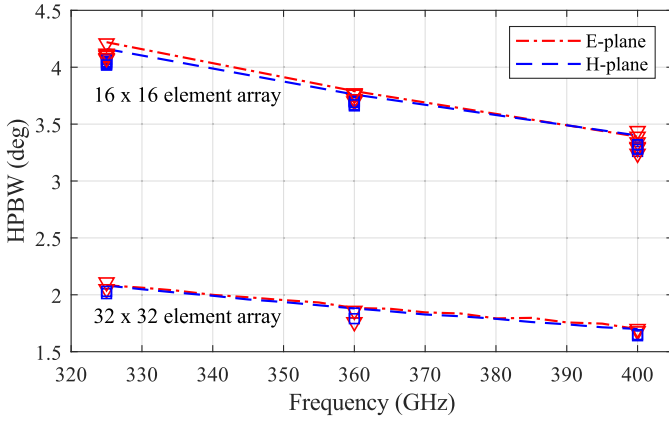
Fig. 14. Measured and simulated HPBW of all the manufactured antennas. E-plane is shown in red, and H-plane is shown in blue. Dashed lines represent the simulated data, and the discrete points are the measured values for each antenna.
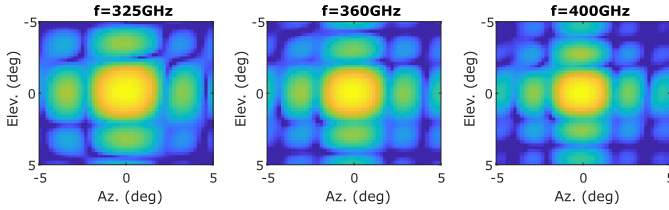

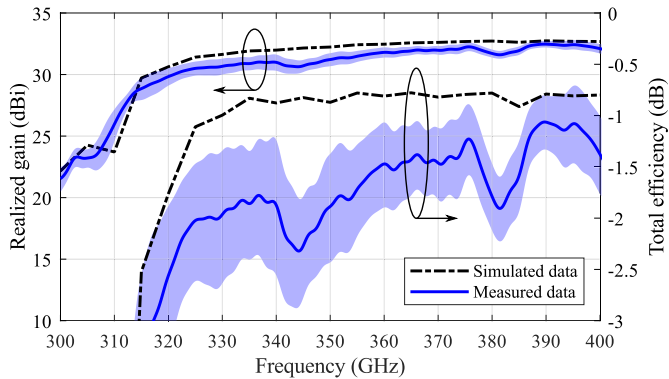Fig. 15. Measured 2-D plots of the main lobe for the 32×32 antenna #2 at three different frequencies.

Fig. 16. Measured and simulated realized gains and total efficiency for the 16×16 element array. Dashed black lines show the simulated data, and blue solid line and shaded blue area show the mean value and the standard deviation ($\pm \sigma$) of the measured data for the six antenna prototypes.

an average total efficiency of -1.5 dB (70%). This efficiency considers both mismatch loss and insertion loss.

The measured and simulated realized gains and radiation efficiency for the two 32×32 element prototypes are depicted in Fig. 17 and are in good agreement. The best-case antenna (antenna #2) has a realized gain that ranges between 36 and 38.2 dBi, showing a total efficiency of around -2.2 dB (60%). The measured efficiency is slightly lower than expected from simulations, which could be due to an increased sidewall roughness during the etching or a reduced metal thickness on the sidewalls.
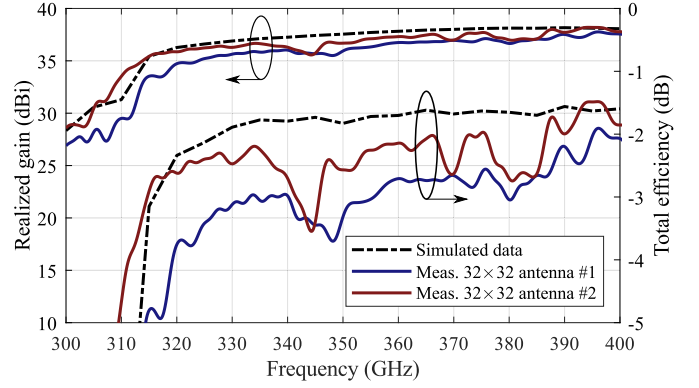

Fig. 17. Measured and simulated realized gains and total efficiency for the two 32×32 element prototypes.
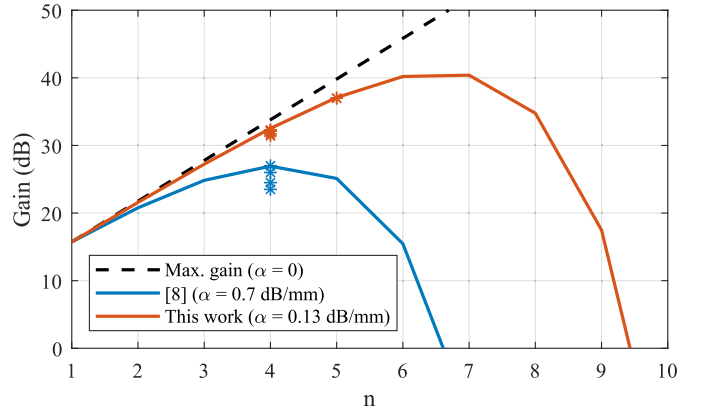

Fig. 18. Gain estimation for a $2^n \times 2^n$ element array considering (1) and (2) and attenuation constant α from gain measurements at 370 GHz. The blue line shows the results from [8], and the red curve shows the results from this article. Individual data points show the measured gain for different manufactured prototypes.

The corporate BFN is the main contributor to the loss in a waveguide array antenna [8], [25] due to the long waveguide sections. This loss is the main limiting factor for the maximum gain that can be achieved with a corporate feed $2^n \times 2^n$ element array, and the maximum theoretical gain as a function of n can be written as

$$IL_{BFN} = \alpha(d_x + d_y) \cdot (2^{n-1} - 1) \qquad (1)$$

$$G_{max} = 10 \cdot log_{10}(4\pi \cdot A_{ap} \cdot \lambda^{-2}) - IL_{BFN} \qquad (2)$$

where IL_{BFN} is the insertion loss of the BFN, α is the attenuation constant in dB/mm of the waveguide, d_x and d_y are the distance between radiating elements in x and y, G_{max} is the maximum theoretical gain, A_{ap} is the aperture area, and λ is the wavelength in free space.

The theoretical value of G_{max} as a function of n is shown in Fig. 18 at 370 GHz for the α values obtained from gain measurements in [8] ($\alpha = 0.6$ dB/mm) and in this article ($\alpha = 0.13$ dB/mm). Each data point shown in the plot represents an antenna prototype that has been manufactured and tested. The curves predict that the SOI micromachining technology presented here can achieve a maximum gain over 40 dBi at 370 GHz with a 64×64 element array antenna. The data in Fig. 18 also show how all the 16×16 element

antenna prototypes have at least 5 dB higher gain than the previously published article [8] with identical aperture size while providing double the operation bandwidth.

V. Conclusion

A high-gain and broadband THz antenna technology has been presented in this article. The low-loss SOI micromachining process used for the fabrication of the antennas is an enabling technology, allowing for the multilayer compact geometries that are needed for the broadband operation. The two designs shown in this article demonstrate 32.8 and 38 dBi gain with an 80 GHz operation bandwidth [22% fractional bandwidth (FBW)] in a low-profile design (the total height of the antennas is below 1.1 mm). In this article we present, to the best of our knowledge, the highest gain antenna reported in the sub-mmW frequency range and above not based in optics (lenses or reflectors).

The eight manufactured prototypes show excellent agreement with the simulation data due to the high uniformity of the micromachining process. In addition, the antennas can be directly mounted on a standard waveguide flange, avoiding the use of complicated and costly CNC-milled test fixtures, custom flanges, or interfaces. Silicon micromachined array antennas can be an attractive alternative to the commonly used reflectors or lenses for point-to-point data links in the THz range since they can provide well-matched, high-gain, and broadband operation as well as high miniaturization.

References

[1] *Mobile Data Traffic Outlook*, Ericsson, Stockholm, Sweden, 2019.

[2] T. Nagatsuma, G. Ducournau, and C. C. Renaud, "Advances in terahertz communications accelerated by photonics," *Nature Photon.*, vol. 10, no. 6, pp. 371–379, Jun. 2016.

[3] S. Koenig *et al.*, "Wireless sub-THz communication system with high data rate," *Nature Photon.*, vol. 7, no. 12, pp. 977–981, Dec. 2013.

[4] H. Wang, X. Dong, M. Yi, F. Xue, Y. Liu, and G. Liu, "Terahertz high-gain offset reflector antennas using SiC and CFRP material," *IEEE Trans. Antennas Propag.*, vol. 65, no. 9, pp. 4443–4451, Sep. 2017.

[5] M. Alonso-Delpino, T. Reck, C. Jung-Kubiak, C. Lee, and G. Chattopadhyay, "Development of silicon micromachined microlens antennas at 1.9 THz," *IEEE Trans. THz Sci. Technol.*, vol. 7, no. 2, pp. 191–198, Mar. 2017.

[6] K. Fan, Z.-C. Hao, Q. Yuan, and W. Hong, "Development of a high gain 325–500 GHz antenna using quasi-planar reflectors," *IEEE Trans. Antennas Propag.*, vol. 65, no. 7, pp. 3384–3391, Jul. 2017.

[7] Z.-C. Hao, J. Wang, Q. Yuan, and W. Hong, "Development of a low-cost THz metallic lens antenna," *IEEE Antennas Wireless Propag. Lett.*, vol. 16, pp. 1751–1754, 2017.

[8] K. Tekkouk *et al.*, "Corporate-feed slotted waveguide array antenna in the 350-GHz band by silicon process," *IEEE Trans. Antennas Propag.*, vol. 65, no. 1, pp. 217–225, Jan. 2017.

[9] H. J. Gibson, B. Thomas, L. Rolo, M. C. Wiedner, A. E. Maestrini, and P. De Maagt, "A novel spline-profile diagonal horn suitable for integration into THz split-block components," *IEEE Trans. THz Sci. Technol.*, vol. 7, no. 6, pp. 657–663, Nov. 2017.

[10] Z.-W. Miao, Z.-C. Hao, Y. Wang, B.-B. Jin, J.-B. Wu, and W. Hong, "A 400-GHz high-gain quartz-based single layered folded reflectarray antenna for terahertz applications," *IEEE Trans. THz Sci. Technol.*, vol. 9, no. 1, pp. 78–88, Jan. 2019.

[11] A. Gomez-Torrent *et al.*, "A low-profile and high-gain frequency beam steering sub-THz antenna enabled by silicon micromachining," *IEEE Trans. Antennas Propag.*, to be published.

[12] B. Beuerle, J. Campion, U. Shah, and J. Oberhammer, "A very low loss 220–325 GHz silicon micromachined waveguide technology," *IEEE Trans. THz Sci. Technol.*, vol. 8, no. 2, pp. 248–250, Mar. 2018.

[13] O. Glubokov, X. Zhao, J. Campion, B. Beuerle, U. Shah, and J. Oberhammer, "Investigation of fabrication accuracy and repeatability of high-Q silicon-micromachined narrowband sub-THz waveguide filters," *IEEE Trans. Microw. Theory Techn.*, vol. 67, no. 9, pp. 3696–3706, Sep. 2019.

[14] A. Gomez-Torrent, U. Shah, and J. Oberhammer, "Compact silicon-micromachined wideband 220–330-GHz turnstile orthomode transducer," *IEEE Trans. THz Sci. Technol.*, vol. 9, no. 1, pp. 38–46, Jan. 2019.

[15] U. Shah, "A 500–750 GHz RF MEMS waveguide switch," *IEEE Trans. THz Sci. Technol.*, vol. 7, no. 3, pp. 326–334, May 2017.

[16] T. Reck, C. Jung-Kubiak, and G. Chattopadhyay, "A 700-GHz MEMS waveguide switch," *IEEE Trans. THz Sci. Technol.*, vol. 6, no. 4, pp. 641–643, Jul. 2016.

[17] U. Shah *et al.*, "Submillimeter-wave 3.3-bit RF MEMS phase shifter integrated in micromachined waveguide," *IEEE Trans. THz Sci. Technol.*, vol. 6, no. 5, pp. 706–715, 2016.

[18] K. Sarabandi, A. Jam, M. Vahidpour, and J. East, "A novel frequency beam-steering antenna array for submillimeter-wave applications," *IEEE Trans. THz Sci. Technol.*, vol. 8, no. 6, pp. 654–665, Nov. 2018.

[19] J. Campion *et al.*, "Toward industrial exploitation of THz frequencies: Integration of SiGe MMICs in silicon-micromachined waveguide systems," *IEEE Trans. THz Sci. Technol.*, vol. 9, no. 6, pp. 624–636, Nov. 2019.

[20] Y. Miura, J. Hirokawa, M. Ando, Y. Shibuya, and G. Yoshida, "Double-layer full-corporate-feed hollow-waveguide slot array antenna in the 60-GHz band," *IEEE Trans. Antennas Propag.*, vol. 59, no. 8, pp. 2844–2851, Aug. 2011.

[21] T. Tomura, J. Hirokawa, T. Hirano, and M. Ando, "A 45° linearly polarized hollow-waveguide 16 × 16-slot array antenna covering 71–86 GHz band," *IEEE Trans. Antennas Propag.*, vol. 62, no. 10, pp. 5061–5067, 2014.

[22] J. Campion, U. Shah, and J. Oberhammer, "Elliptical alignment holes enabling accurate direct assembly of micro-chips to standard waveguide flanges at sub-THz frequencies," in *IEEE MTT-S Int. Microw. Symp. Dig.*, Jun. 2017, pp. 1262–1265.

[23] A. R. Conn, N. I. Gould, and P. L. Toint, *Trust Region Methods* (MPS-SIAM Series on Optimization). Philadelphia, PA, USA: Society for Industrial and Applied Mathematics, 2000.

[24] K. Fujii, K. Sakai, T. Sugiyama, K. Sebata, and I. Nishiyama, "Calibration of EMI antennas for microwave frequency bands by the extrapolation technique," *J. Nat. Inst. Inf. Commun. Technol.*, vol. 63, no. 1, pp. 105–116, 2016.

[25] J. W. Jordan *et al.*, "Monolithically fabricated 4096-element, PolyStrata broadband D-band array demonstrator," in *IEEE MTT-S Int. Microw. Symp. Dig.*, Jun. 2019, pp. 1060–1063.

Adrian Gomez-Torrent (Graduate Student Member, IEEE) was born in Artariain, Spain, in 1990. He received the B.Sc. and M.Sc. degrees from the Public University of Navarra (UPNA), Pamplona, Spain, in 2014.

From 2013 to 2017, he was with the Antennas and Microwave Components Groups, UPNA, where he was involved with microwave passive devices and silicon micromachining for RF/terahertz (THz) components. Since 2017, he has been with the Division of Micro and Nanosystems, KTH Royal Institute of Technology, Stockholm, Sweden. His research interests include silicon micromachining for microwave and sub-THz passive waveguide components, antennas, and switching matrices for beam-steering applications.
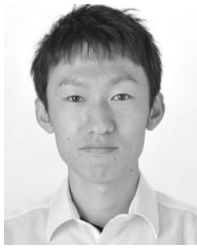
Takashi Tomura (Member, IEEE) received the B.S., M.S., and D.E. degrees in electrical and electronic engineering from the Tokyo Institute of Technology, Tokyo, Japan, in 2008, 2011, and 2014, respectively.

He was a Research Fellow with the Japan Society for the Promotion of Science (JSPS), Tokyo, Japan, in 2013. From 2014 to 2017, he worked at Mitsubishi Electric Corporation, Tokyo, and was engaged in Research and Development of aperture antennas for satellite communications and radar systems. From 2017 to 2019, he was a Specially Appointed Assistant Professor with the Tokyo Institute of Technology, Tokyo, where he is currently an Assistant Professor. His research interests include electromagnetic analysis, aperture antennas, and planar waveguide slot array antennas.

Dr. Tomura is a member of the IEICE. He received the Best Student Award from Ericsson Japan in 2012, the IEEE AP-S Tokyo Chapter Young Engineer Award in 2015, and the Young Researcher Award from IEICE Technical Committee on Antennas and Propagation in 2018.

Wataru Kuramoto received the B.S. degree in electrical and electronic engineering from the Tokyo Institute of Technology, Tokyo, Japan, in 2019, where he is currently pursuing the M.S. degree.

Jiro Hirokawa (Fellow, IEEE) received the B.S., M.S., and D.E. degrees in electrical and electronic engineering from the Tokyo Institute of Technology (Tokyo Tech), Tokyo, Japan, in 1988, 1990, and 1994, respectively.

He was a Research Associate with Tokyo Tech from 1990 to 1996. He was with the antenna group of Chalmers University of Technology, Gothenburg, Sweden, as a Post-Doctoral Fellow from 1994 to 1995. He was an Associate Professor from 1996 to 2015 with Tokyo Tech, where he is currently a Professor. His research area has been in slotted waveguide array antennas and millimeter-wave antennas.

Prof. Hirokawa is a fellow of IEICE. He received the IEEE AP-S Tokyo Chapter Young Engineer Award in 1991, the Young Engineer Award from IEICE in 1996, the Tokyo Tech Award for Challenging Research in 2003, the Young Scientists' Prize from the Minister of Education, Cultures, Sports, Science and Technology, Japan, in 2005, the Best Paper Award in 2007, the Best Letter Award in 2009 from IEICE Communications Society, and the IEICE Best Paper Award in 2016 and 2018.

Issei Watanabe received the B.E., M.E., and Ph.D. degrees in engineering science from Osaka University, Suita, Japan, in 1999, 2001, and 2005, respectively.

From 2001 to 2004, he joined collaboration team among Osaka University, Suita, Japan, Communications Research Laboratory (CRL), Tokyo, Japan, and Fujitsu Laboratories Ltd., Atsugi, Japan, where he worked on growth of epitaxial heterostructure by molecular beam epitaxy (MBE) and fabrication and characterization of cryogenically cooled InP-based InGaAs/InAlAs HEMTs. In 2004, he joined the National Institute of Information and Communications Technology (NICT; formerly CRL), Tokyo, Japan, where he has been involved in the research and development of nanoscale gate compound semiconductor electron devices and circuits, and high-frequency measurement technology for millimeter- and terahertz (THz)-wave applications.

Dr. Watanabe is a member of the Japan Society of Applied Physics and the Institute of Electronics and Information and Communication Engineers (IEICE).

Akifumi Kasamatsu received the B.E., M.E., and Ph.D. degrees in electronics engineering from Sophia University, Tokyo, Japan, in 1991, 1993, and 1997, respectively.

From 1997 to 1999, he was a Research Assistant with Sophia University. From 1999 to 2002, he was with Fujitsu Laboratories Ltd., Atsugi, Japan. Since 2002, he has been with the National Institute of Information and Communications Technology (NICT), Koganei, Japan, where he is currently working as an Executive Researcher and a Principal Investigator of the terahertz (THz) wave electronics project. His current research interests are in wireless communication technology such as wireless transceivers and nanoscale semiconductor devices for millimeter-wave and THz wave communications.

Dr. Kasamatsu is a member of the Institute of Electronics, Information and Communication Engineers (IEICE), Japan, and Japanese Society of Applied Physics (JSAP). He received the 28th Meritorious Award on Radio presented by the Association of Radio Industries and Businesses of Japan, the 2019 Maejima Hisoka Award presented by the Post and Telecom Association of Japan, the 2016 MTT International Microwave Symposium Best Industry Paper Award, and the 2015 and 2017 Radio Frequency Integrated Technology (RFIT) Awards.

Joachim Oberhammer (Senior Member, IEEE) was born in Brunico, Italy, in 1976. He received the M.Sc. degree in electrical engineering from the Graz University of Technology, Graz, Austria, in 2000 and the Ph.D. degree from the KTH Royal Institute of Technology, Stockholm, Sweden, in 2004.

He was a Post-Doctoral Research Fellow with Nanyang Technological University, Singapore, in 2004 and with Kyoto University, Kyoto, Japan, in 2008. He was leading radio frequency/microwave/terahertz (THz) microelectromechanical systems research at KTH Royal Institute of Technology till 2010, was an Associate Professor till 2015, and now working as a Professor in microwave and THz microsystems. He was a Guest Researcher with Nanyang Technological University, in 2007 and NASA Jet Propulsion Laboratory, Pasadena, CA, USA, in 2014. He has authored or coauthored more than 100 reviewed research articles. He holds four patents.

Dr. Oberhammer served as a TPRC member of IEEE Transducers 2009 and 2015, the IEEE International Microwave Symposiums 2010–2016, IEEE Micro Electro Mechanical Systems 2011 and 2012, and IEEE Radio and Wireless Week 2015 and 2016. He has been a Steering Group member of the IEEE MTT-S and AP-S Chapters Sweden since 2009. Since 2014, he has been a Steering Group member of the Young Academy of Sweden. He was a recipient of an award by the Ericsson Research Foundation, a grant by the Swedish Innovation Bridge, and a scholarship by the Japanese Society for the Promotion of Science, in 2004, 2007, and 2008, respectively. The research work he is heading received six Best Paper Awards (five of which at IEEE conferences) and four IEEE Graduate Fellowship Awards (by the IEEE MTT-S and by AP-S) since 2009. In 2013, he received an ERC Consolidator Grant by the European Research Council.